Novel lead-free BCZT-based ceramic with thermally-stable recovered energy density and increased energy storage efficiency

Zouhair Hanani, Soukaina Merselmiz, M'barek Amjoud, Daoud Mezzane, Mohammed Lahcini, Jaafar Ghanbaja, Matjaž Spreitzer, Damjan Vengust, Mimoun El Marssi, Igor A. Luk'Yanchuk, et al.

▶ **To cite this version:**

Zouhair Hanani, Soukaina Merselmiz, M'barek Amjoud, Daoud Mezzane, Mohammed Lahcini, et al.. Novel lead-free BCZT-based ceramic with thermally-stable recovered energy density and increased energy storage efficiency. Journal of Materiomics, 2022, 8 (4), pp.873-881. ⟨10.1016/j.jmat.2021.12.011⟩. ⟨hal-03716479⟩

HAL Id: hal-03716479

https://hal.science/hal-03716479v1

Submitted on 7 Jul 2022

HAL is a multi-disciplinary open access archive for the deposit and dissemination of scientific research documents, whether they are published or not. The documents may come from teaching and research institutions in France or abroad, or from public or private research centers.

L'archive ouverte pluridisciplinaire **HAL**, est destinée au dépôt et à la diffusion de documents scientifiques de niveau recherche, publiés ou non, émanant des établissements d'enseignement et de recherche français ou étrangers, des laboratoires publics ou privés.

HAL Authorization

Journal of Materiomics xxx (xxxx) xxx

Contents lists available at ScienceDirect

Journal of Materiomics

journal homepage: www.journals.elsevier.com/journal-of-materiomics/

Research paper

Novel lead-free BCZT-based ceramic with thermally-stable recovered energy density and increased energy storage efficiency

Zouhair Hanani [a, b, c, *], Soukaina Merselmiz [a], M'barek Amjoud [a], Daoud Mezzane [a, d], Mohammed Lahcini [a, e], Jaafar Ghanbaja [f], Matjaž Spreitzer [c], Damjan Vengust [c], Mimoun El Marssi [d], Igor A. Luk'yanchuk [d, g], Zdravko Kutnjak [c], Brigita Rožič [c], Mohamed Gouné [b]

[a] IMED-Lab, Cadi Ayyad University, Avenue Abdelkrim El Khattabi, P.B. 549, Marrakesh, 40000, Morocco
[b] ICMCB, University of Bordeaux, 87 Avenue Du Dr Albert Schweitzer, Pessac, 33600, France
[c] Jozef Stefan Institute, Jamova Cesta 39, Ljubljana, 1000, Slovenia
[d] LPMC, University of Picardy Jules Verne, 33 Rue Saint Leu, Amiens, 80039, France
[e] Mohammed VI Polytechnic University, Lot 660-Hay Moulay Rachid, Ben Guerir, 43150, Morocco
[f] IJL, University of Lorraine, 54000, Nancy, France
[g] Department of Building Materials, Kyiv National University of Construction and Architecture, Kyiv, 03680, Ukraine

ARTICLE INFO

Article history:
Received 24 November 2021
Received in revised form
27 December 2021
Accepted 31 December 2021
Available online xxx

Keywords:
Lead-free ceramics
Low temperature
Piezoelectric
Thermal stability
Energy storage
Nanostructuration

ABSTRACT

The eco-responsible lead-free piezoelectric ceramics have been intensively searched for more than a decade, however, the final goal to replace toxic ceramics like lead zirconate titanate (PZT) with lead-free compounds, having comparable or even better performance has not yet been reached. In this road, the lead-free ceramics $Ba_{0.85}Ca_{0.15}Zr_{0.1}Ti_{0.9}O_3$ (BCZT), possessing excellent dielectric, ferroelectric, and piezoelectric properties are regarded as serious candidates for the PZT replacement. Besides, nanostructuring BCZT is of paramount importance to enhance these functionalities even more. Here, BCZT multipodes are designed by template-growth hydrothermal synthesis using hydrogen zirconate titanate nanowires. We demonstrate that the fabricated BCZT multipodes exhibit high dielectric permittivity of 5300 with a temperature stability coefficient of ±5.9% between 20 and 140 °C. A significant recovered energy density of 315.0 mJ/cm^3 with high thermal stability and high energy storage efficiency of 87.4%, and enhanced large-signal piezoelectric coefficient d^*_{33} (310 pm/V) are found. Compared to the traditional BCZT ceramics reported in the literature, relying on high-temperature processing, our sample exhibits boosted energy storage parameters at a much lower temperature. These outcomes may offer a new strategy to tailor eco-responsible relaxor ferroelectrics toward superior energy storage performance for ceramic capacitor applications.

© 2022 The Chinese Ceramic Society. Production and hosting by Elsevier B.V. This is an open access article under the CC BY-NC-ND license (http://creativecommons.org/licenses/by-nc-nd/4.0/).

1. Introduction

Today's piezoelectric devices market is dominated mainly by ceramic materials based on lead zirconate titanate (PZT) systems because of their excellent piezoelectric properties [1–3]. These piezo-materials are primarily used in sensors, actuators, electronics and non-volatile ferroelectric memory and transistor devices [4–7]. Nevertheless, due to growing environmental concerns on the toxicity of lead-based piezoelectrics, the replacement of Pb-based materials by homologs with comparable piezoelectric properties but without lead is an emergent task [2,8–13]. Since 2009, $Ba_{0.85}Ca_{0.15}Zr_{0.1}Ti_{0.9}O_3$ (BCZT) material has aroused considerable attention for such replacement due to its excellent dielectric, ferroelectric and piezoelectric properties [14]. BCZT ceramic is a promising innovative material for energy storage and energy harvesting applications [15–21]. However, most published works are based on BCZT 0D-particles due to their simple synthesis procedures [16,20,22–24]. However, the most fascinating ferroelectric and piezoelectric properties are typically found in 1D, 2D, and 3D

* Corresponding author. Jozef Stefan Institute, Jamova Cesta 39, Ljubljana, 1000, Slovenia.
E-mail address: zouhair.hanani@ijs.si (Z. Hanani).
Peer review under responsibility of The Chinese Ceramic Society.

https://doi.org/10.1016/j.jmat.2021.12.011
2352-8478/© 2022 The Chinese Ceramic Society. Production and hosting by Elsevier B.V. This is an open access article under the CC BY-NC-ND license (http://creativecommons.org/licenses/by-nc-nd/4.0/).

Please cite this article as: Z. Hanani, S. Merselmiz, M. Amjoud *et al.*, Novel lead-free BCZT-based ceramic with thermally-stable recovered energy density and increased energy storage efficiency, Journal of Materiomics, https://doi.org/10.1016/j.jmat.2021.12.011

nanomaterials with more complex morphologies [25–30]. Zhou *et al.* prepared BCZT nanowires via two-steps hydrothermal processing. They found that the peak power density could be enhanced nine times using BCZT nanowires instead of BCZT nanoparticles [31]. Previously, we reported BCZT ceramics with rod-like grains, elaborated by surfactant-assisted solvothermal processing, having excellent electrical properties and large electrocaloric effect [25].

To further tune the dielectric properties of BCZT ceramics, Chary *et al.* reported the dielectric properties of large aspect ratio BCZT nanofibers mat fabricated using electro-spinning technique [32]. The authors stated very low dielectric permittivity ($\varepsilon_r \approx 200$) and relatively higher Curie temperature ($T_C = 108$ °C) in BCZT nanofibers compared to the bulk ceramics ($T_C = 90$ °C). Another attempt to enhance T_C was reported by Datta *et al.* in BCZT nanowires prepared by porous template-assisted sol-gel synthesis [33]. A very high T_C of about 300 °C was reached, though thermally and frequency unstable dielectric ε_r and moderate ferroelectric properties were obtained.

Despite the high dielectric constant values obtained in BCZT or other $BaTiO_3$-based ceramics ($\varepsilon_r \geq 10000$), the thermal stability of the dielectric properties over a wide temperature range still questioned due to the narrow peak of the dielectric permittivity around the ferroelectric–paraelectric phase transition [34]. To mitigate this weakness, most researchers rely on the search for the appropriate mixture, at high temperature, of BCZT with other stabilizing powders exhibiting the enhanced ferro-, piezo-, and paraelectric parameters. However, no reliable way of temperature stabilization of the dielectric permittivity was suggested. Usually, the BCZT or even $BaTiO_3$-based ceramics are combined with other lead-free materials like $Bi_{0.5}Na_{0.5}TiO_3$-based ceramics due to their high thermal stability of the dielectric permittivity over a broad temperature range. However, a dramatic drop of the dielectric permittivity ($\varepsilon_r < 1500$) is usually observed [35,36].

From the energy storage view, $BaTiO_3$-based ceramics are the most attractive candidates for high energy density storage applications. Particularly, combining $BaTiO_3$ (BT) with $Bi(Mg_{0.5}Ti_{0.5})O_3$ [37], $Bi(Mg_{2/3}Nb_{1/3})O_3$ [38], $Bi_{2/3}(Mg_{1/3}Nb_{2/3})O_3$ [39] and $Na_{0.5}Bi_{0.5}TiO_3$ [40] is a common strategy to induce high dielectric breakdown strength and phase transition from ferroelectric to relaxor ferroelectric in BT. For instance, Liu *et al.* designed $Bi(Mg_{2/3}Nb_{1/3})O_3$-modifed BT ceramics with improved temperature and frequency stability, high recoverable energy density (W_{rec}) of ~1.89 J/cm^3, an relatively high efficiency (η) of ~83% [38]. Besides, Yang *et al.* reported lead-free relaxor $BaTiO_3$–$0.06Bi_{2/3}(Mg_{1/3}Nb_{2/3})O_3$ ceramics with W_{rec} of ~4.55 J/cm^3 with η ~90% at ~520 kV/cm [39]. Unfortunately, despite achieving enhanced energy storage properties, high temperatures (>1000 °C) are required during the fabrication of these materials [41,42]. Accordingly, obtaining improved energy storage parameters at lower temperatures (<200 °C) is a challenging task. Recently, we reported the hydrothermal growth of lead-free BCZT nanostructured multipods using $H_2(Zr_{0.1}Ti_{0.9})_3O_7$ (HZTO) inorganic template at 180 °C, where no single-phase BCZT was obtained, and HZTO and Zr-doped $CaTiO_3$ (CZTO) phases were always found next to BCZT one [43]. Such an approach is favorable because one can couple the well-known properties of BCZT with those of $CaTiO_3$. Indeed, it was reported that the linear dielectric ceramics $CaTiO_3$ exhibit very promising energy storage performances [44,45]. Particularly, Zr-doped $CaTiO_3$ (CZTO) ceramics own high-thermal stability of the dielectric permittivity and the energy storage density [46–48].

In this paper, we suggest a conceptually innovative strategy to tune the electrical properties of BCZT by nanostructuring. We used the low-temperature hydrothermal synthesis and demonstrated its effectiveness to design complex morphologies like wires, cubes, and multipods for energy storage applications. Notably, we found that the co-existence of the ferroelectric BCZT multipods and the paraelectric Zr-doped $CaTiO_3$ cubes enhanced the relaxor behavior of the fabricated nanosystem and resulted in the desirable thermally-stable dielectric permittivity and improved energy storage performances compared to other reported BCZT ceramics.

2. Experimental procedures

2.1. Preparation of BCZT multipods

To design nanostructured lead-free BCZT multipods, $Zr_{0.1}Ti_{0.9}O_2$ (ZTO) powder was synthesized by the sol-gel method as reported in [22]. Then, two-steps hydrothermal processing was used. The first step involves the elaboration of the $H_2(Zr_{0.1}Ti_{0.9})_3O_7$ nanowires (HZTO-NWs), which serve as an inorganic template for BCZT preparation. For this purpose, 5 g of ZTO powder, was dispersed in 100 mL of 10 M NaOH aqueous solution for 1 h, then the slurry was transferred to a 150 mL-Teflon-lined stainless-steel autoclave. After sealing and heating at 240 °C for 48 h, the autoclave was cooled down to room temperature, and the resulting white suspension ($Na_2(Zr_{0.1}Ti_{0.9})_3O_7$, NaZTO) was collected by filtration and soaked in 0.2 M HCl for 10 h to convert NaZTO to HZTO. The obtained product was washed several times with deionized water and ethanol using repeated centrifugation at 4000 rpm for 10 min, filtered, then freeze-dried for 48 h to obtain a fluffy product. For the BCZT multipods preparation, 150 mg of HZTO-NWs was dispersed in 35 mL of barium acetate (50 mM) and calcium nitrate tetrahydrate (8.8 mM) and 0.1 M of potassium hydroxide solution. Subsequently, the suspension was sonicated for 10 min to break the agglomeration, purged with N_2, transferred into a 50 mL-Teflon-lined stainless-steel autoclave, sealed and heated at 180 °C for 24 h. After the hydrothermal reaction was completed, the sealed autoclave was cooled down to room temperature. The resulting white precipitate was collected by centrifugation at 5000 rpm for 10 min, soaked in 0.2 M HCl for 4 h, and washed several times with 0.2 M HCl, deionized water and ethanol, and finally dried at 80 °C for 12 h. The prepared sample is designated as 50B24h.

2.2. Characterizations

The room-temperature crystalline structure of the prepared powder was determined by X-ray diffraction (XRD, Rigaku SmartLab) using a step angle of 0.012° in the 2θ range from 5 to 80° and Cu-Kα radiation ($\lambda \approx 1.54059$ Å). The morphology observations were analyzed using a scanning electron microscope equipped with an electron gun (FESEM, JEOL JSM-7600F). Transmission electron microscope (JEOL - ARM 200F Cold FEG TEM/STEM) operating at 200 kV coupled with an energy-dispersive X-ray spectrometer (EDX) was used to confirm the composition of the nanowires, cubes and multipods. To gain insight into the structural, morphological, and electrical properties, 50B24h powder was sintered at 1250 °C for 10 h in air. Raman spectroscopy was employed to determine the structural properties change in 50B24h ceramic from 0 to 200 °C. For this purpose, the 50B24h sample was excited using an argon laser's polarized radiation ($\lambda = 514.5$ nm), and the Raman spectra were recorded using a Renishaw inVia Reflex spectrometer. Moreover, a well-calibrated Linkam heating-cooling stage with temperature stability of 0.1 K was utilized to control sample temperature. To compare the spectra obtained at various temperatures, a Bose-Einstein correction has been performed. The sintered pellet's surface morphology and composition ere characterized by field emission scanning electron microscope (FESEM, JEOL JSM-7600F) equipped with a backscattered electrons (BSE) detector under 10 kV. The semi-quantification elemental analysis to identify the weight percentage of major and minor elements present in the

sintered ceramic was done using the OXFORD INCA energy dispersive X-ray spectrometer. The dielectric properties of gold-sputtered 50B24h pellet in the frequency range of 20 Hz to 1 MHz were measured using a precision LCR Meter (HP 4284A, 20 Hz to 1 MHz) from 20 to 200 °C. The polarization–electric field (*P–E*) and strain–electric field (*S–E*) hysteresis loops of the 50B24h sample, with a thickness of 300 μm, were measured using a ferroelectric test system (AiXACCT, TF Analyzer 2000) equipped with a high-voltage amplifier (TREK model 609E-6) in a silicone oil bath. The *P–E* loops were performed using triangular voltage waveforms at a frequency of 10 Hz at room temperature at different electric fields (10–60 kV/cm) and in the temperature range of 20–160 °C with a 20 °C step at 60 kV/cm.

3. Results and discussions

3.1. Structural, morphology and composition properties of 50B24h sample

As seen in Fig. 1a, the 50B24h powder is composed of nanowires, cubes and multipods. Meanwhile, the EDX analyses of the 50B24h powder prove that the nanowires, cubes and multipods are HZTO, $CaZr_yTi_{1-y}O_3$ (CZTO) and BCZT phases, respectively (Fig. 1b, c). The XRD pattern of 50B24h powder is illustrated in Fig. 1g, where the presence of BCZT, HZTO, and CZTO and $Ca_3(Zr_yTi_{1-y})_2O_7$ ($C_3(ZT)_2O_7$) phases is observed. The XRD pattern can be indexed to monoclinic (*C2/m*), orthorhombic (*Pbnm*), orthorhombic (*Ccm2₁*) and tetragonal (*P4mm*) for HZTO, CZTO, $C_3(ZT)_2O_7$ and BCZT phases, respectively. The amounts of BCZT, HZTO, CZTO and $C_3(ZT)_2O_7$ phases were determined using the Rietveld quantification tool in HighScore Plus software and reference structure data from the Crystallography Open Database (COD) 2020 and were found to be 58, 7, 18, and 17%. Further structural, morphology and composition analyses can be found in [43].

To gain insight into the morphological properties of these mixed morphologies at high temperature, 50B24h powder was sintered at 1250 °C for 10 h (Fig. 1d). We recall that before sintering, the powder was composed of nanowires, cubes, and multipods. Hence, backscattered electrons (BSE) detector was used to visualize the composition fluctuation and gain intuitions of the nature of the observed regions after the sintering process (Fig. 1e, f), and an EDX spectrometer was employed to have a semi-quantitative analysis of the composition of each phase. As a result, it was found that the darkest regions correspond to $CaZr_yTi_{1-y}O_3$ (CZTO) and/or $Ca_3(Zr_yTi_{1-y})_2O_7$ ($C_3(ZT)_2O_7$) phases, and the brightest ones correspond to the BCZT phase. The bulk density of 50B24h ceramic was measured by Archimedes method and found to be 5.15 g/cm^3, corresponding to a relative density of 90%.

Memo	O	Ca	Ti	Zr	Ba	Total (Mole fraction (%))
1	64.28	-	34.33	1.39	-	100
2	70.5	-	28.97	0.53	-	100
3	59.63	1.03	19.05	0.62	19.67	100
4	55.48	1.02	21.52	0.55	21.43	100
5	49.79	1.73	24.07	0.64	23.77	100
6	54.75	0.68	21.94	0.82	21.82	100
7	47.94	24.36	25.07	2.63	-	100
8	61.49	19.02	17.89	1.6	-	100
9	62.76	0.34	34.24	0.83	1.83	100
10	64.43	-	34.28	1.29	-	100

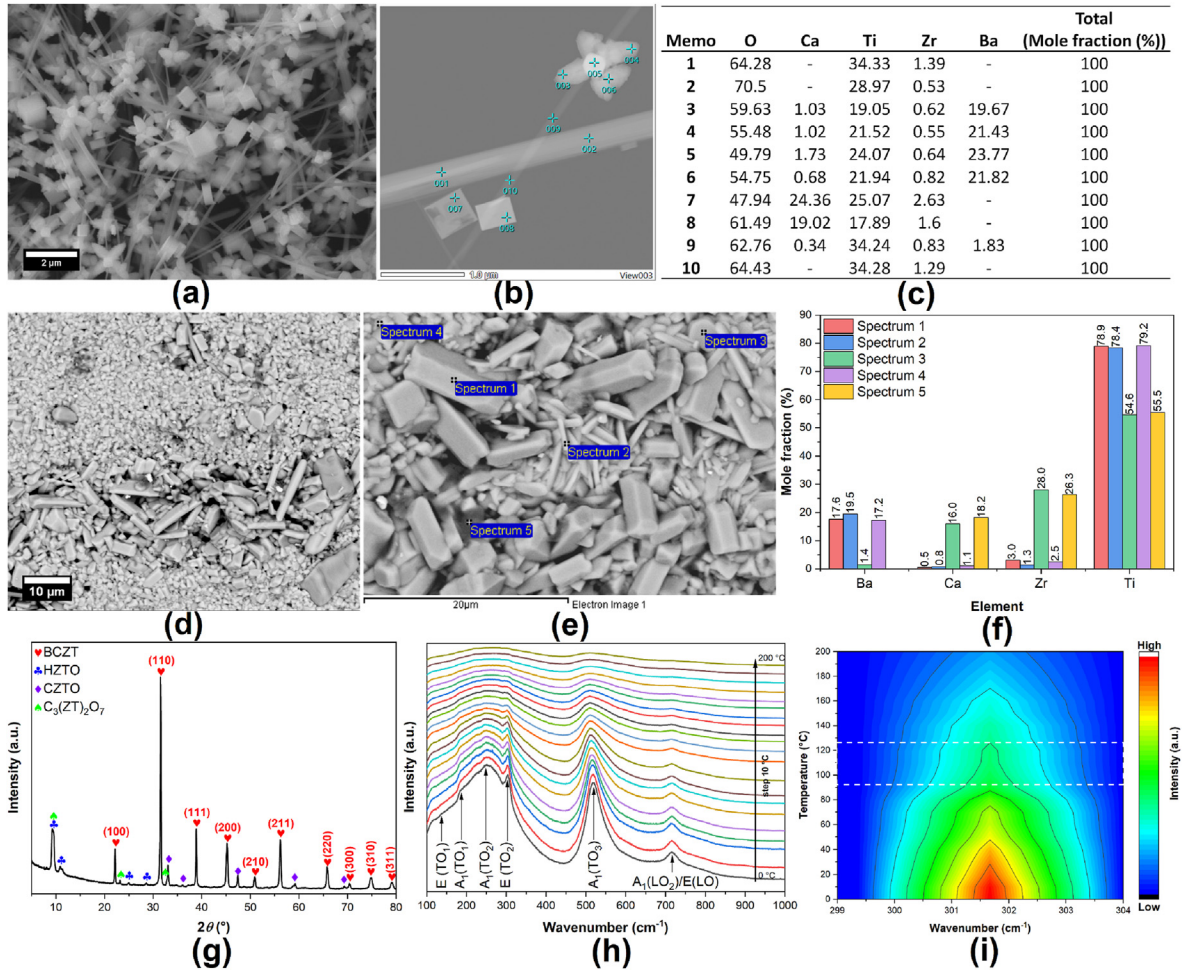

Fig. 1. Structural, morphology and composition properties of 50B24h sample. (a) FESEM and (b) TEM images of the 50B24h powder, and (c) results of the EDX analyses at different spots. (d) BSE-FESEM micrograph of the surface of the sintered ceramic. (e) Magnified BSE-FESEM image showing the contrast difference for EDX analysis and (f) EDX results showing the Mole fraction (%) of Ba, Ca, Zr and Ti elements at different spots. (g) Room temperature XRD pattern, (h) thermal evolution of the Raman spectra, and (i) 2D color map of $E(TO_2)$ Raman mode of 50B24h ceramic.

To further investigate the structural properties of the 50B24h sample, Raman spectroscopy was used. It was stated that Raman modes are highly affected by temperature; hence, their thermal evolution could provide ideas about the structural changes upon sample heating. Accordingly, the structural properties of 50B24h ceramic were thoroughly investigated by temperature-dependence Raman spectroscopy from 0 to 200 °C, and the results are depicted in Fig. 1h. At low temperatures, the most intensive Raman peaks are 140, 190, 255, 300, 520, and 720 cm^{-1}, which correspond to E(TO_1), $A_1(TO_1)$, $A_1(TO_2)$, E(TO_2), $A_1(TO_3)$, and $A_1(LO_2)$/E(LO), respectively. These peaks are considered as the peak characteristics of perovskite oxides [49]. Besides, the triple modes E(TO_1), $A_1(TO_2)$ and $A_1(TO_3)$ are observed and associated with the ferroelectric phase [50]. With the temperature increasing, E(TO_1), $A_1(TO_2)$, $A_1(TO_3)$ and E(TO_2) modes are progressively decreasing, which indicates the approach to the ferroelectric–paraelectric phase transition [20,51]. This structural change was revealed through the 2D color map in the wavenumber around 292–296 $cm^{-1,}$ and temperature between 0 and 200 °C is plotted in Fig. 1i. It is observed that the low-temperature data has a much greater signal and lower background than the high-temperature data. Besides, the intensity of E(TO_2) mode decreases with increasing temperature, and an abrupt intensity change in this mode has occurred between 90 and 130 °C (marked by the dashed rectangle) due to the structural change from ferroelectric (tetragonal) to paraelectric (cubic) phase [15,20,52].

3.2. Dielectric properties of 50B24h sample

The temperature-dependence of the dielectric permittivity (ε_r) and the dielectric loss (*tan* δ) of 50B24h sintered ceramic, between 20 and 200 °C at various frequencies, are plotted in Fig. 2a. A non-usual behavior of the dielectric permittivity is noticed, where ε_r exhibits slightly constant values from room-temperature to T_C, especially at low frequencies, then gradually decreases due to the tetragonal–cubic (*T–C*) phase transition [53,54]. This behavior could be due to the presence of CZTO and $C_3(ZT)_2O_7$ phases in 50B24h powder, which could generate two locally coexisting polar nanoregions (PNRs) of different phases, similar to $Bi_{0.5}Na_{0.5}TiO_3$-based lead-free relaxor ferroelectrics [55]. Besides, the bump around 40 °C corresponds to orthorhombic–tetragonal (*O–T*) phase transition. Furthermore, the detailed analysis of temperature dependence Raman spectroscopy can evidence the *O–T* and *T–C* phase transitions [56,57]. Fig. 2b presents the dielectric permittivity's thermal evolution at 1 kHz with the peak positions of the E(TO_2) Raman mode. The three apparent Raman shift plateaus correspond to the *O*, *T* and *C* phases, respectively, and the two drops match the *O–T* and *T–C* phase transitions. It is worthy to note that with increasing frequency, the maximum of ε_r decreases, and T_c shifts toward higher temperatures (Fig. 2a), indicating a relaxor behavior with strong frequency dispersion [58,59].

The ferroelectric materials follow the *Curie-Weiss* law in the paraelectric phase, as given in Eq. (1) [60]. The thermal evolution of the inverse of ε_r at 1 kHz was fitted using the *Curie-Weiss* law and plotted in Fig. 2c. Where ε_r is the dielectric permittivity, T_0 is the *Curie-Weiss* temperature, and *C* is the *Curie-Weiss* constant.

$$\frac{1}{\varepsilon_r} = \frac{T - T_0}{C} (T > T_0) \quad (1)$$

Here $\Delta T_m(K) = T_{dev} - T_m$ designates the degree of deviation of the ε_r from the *Curie-Weiss* law above T_C, where T_{dev} is the

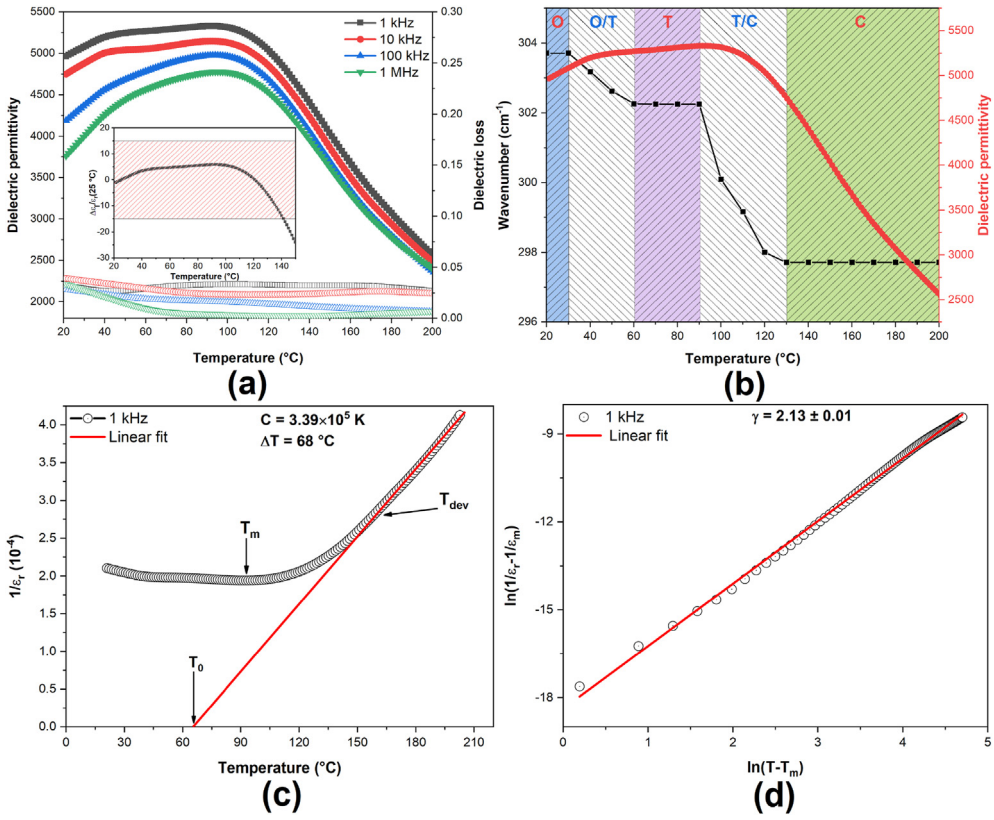

Fig. 2. Dielectric properties of 50B24h ceramic. (a) Temperature-dependence of ε_r and *tan* δ (in the inset the thermal stability of ε_r between 20 and 150 °C), (b) thermal evolution of ε_r at 1 kHz and E(TO_2) mode peak position, plots of (c) the inverse ε_r as a function of temperature determining the *Curie-Weiss* constant *C* at 1 kHz, and (d) the *ln* $(1/\varepsilon - 1/\varepsilon_m)$ *vs ln* $(T - T_m)$ determining the degree of diffuseness γ of the 50B24h ceramic.

temperature at which ε_r starts to deviate from the *Curie-Weiss* law and T_m is the temperature at which ε_r reached the maximum. The Curie constant value is in the order of 10^5 K, which indicates that the high-temperature paraelectric phase of 50B24h ceramic is driven by a displacive-type ferroelectric such as $BaTiO_3$. These parameters are tabulated in Table 1. The diffuseness associated with the ferroelectric–paraelectric phase transition could be determined via the fit of the modified *Curie-Weiss* law as written in Eq. (2) [61]. The fitting results are plotted in Fig. 2d.

$$\frac{1}{\varepsilon_r}-\frac{1}{\varepsilon_m}=\frac{(T-T_0)^{\gamma}}{C}\,(1<\gamma<2) \tag{2}$$

where ε_m denotes the maximum dielectric permittivity and γ refers to the degree of diffuseness of the phase transition. The limiting values $\gamma = 1$ and $\gamma = 2$ characterizes the typical ferroelectric behavior following the *Curie-Weiss* law and the ideal relaxor ferroelectric, respectively. 50B24h ceramic exhibits a degree of transition diffuseness of 2.13 and the considerable value of the degree of deviation from *Curie-Weiss* law (ΔT_m) of 68 °C, indicating a strong diffused phase transition. These values are larger than those reported in BCZT ceramics [16,54,62–64]. Note that $\gamma > 2$ is theoretically possible; it just means that the permittivity at higher temperatures drops off faster than predicted by the power law with $\gamma = 2$ [65]. These results prove the enhanced relaxor behavior and strong diffuse phase transition of 50B24h ceramic [66].

To quantitatively evaluate the temperature stability of the dielectric permittivity, the variation of ε_r at 1 kHz of 50B24h ceramic between 20 and 140 °C was calculated, in the benchmark of 25 °C, by Eq. (3) [35]. While most of $BaTiO_3$-derived ceramics exhibit a narrow peak of the dielectric permittivity at T_C with huge $\Delta\varepsilon_r/\varepsilon_r(25\ ^\circ C)$ variation [34], a stable dielectric permittivity of 50B24h ceramic was observed. According to the X7R specifications, where the temperature variation of capacitance is within ±15% from −55 to 125 °C [67], the 50B24h ceramic can fulfil the X7R specifications at least from 20 to 140 °C with $-14.9\% \le \Delta\varepsilon_r/\varepsilon_r(25\ ^\circ C) \le 5.9\%$. This induces a low $\Delta\varepsilon_r/\varepsilon_r(25\ ^\circ C)$ value of ±5.9% in 50B24h sample compared to other lead-free ceramics between 20 and 130 °C [68–70]. Indeed, the combination of $BaTiO_3$-based ceramics with other solid solutions like $Bi(Mg_{2/3}Ta_{1/3})O_3$ and $Bi_{0.5}Na_{0.5}TiO_3$ well recognized for their thermally-stable dielectric permittivity over a broad temperature range, usually induce low dielectric permittivity (<2000) [35,36]. On the other hand, Ma *et al.* reported thermally stable $BaTiO_3$–$Bi(Mg_{2/3}Ta_{1/3})O_3$ ceramic in the temperature range 30–150 °C but with ε_r of 2000 [68]. Besides, Zhou *et al.* stated the temperature stability of $(Ni_{1/3}Nb_{2/3})^{4+}$ complex-ion modified $Ba_{0.85}Ca_{0.15}Zr_{0.10}Ti_{0.90}O_3$ between −55 to 160 °C but with very low dielectric permittivity of 600 [71]. In addition, Dong *et al.* reported the thermal stability of $0.84BaTiO_3$–$0.16Bi(Ni_{2/3}Ta_{1/3})O_3$ between −77.1 and 156 °C, but also a very-low ε_r of 900 was found [69]. Accordingly, the 50B24h ceramic can operate efficiently from 20 to 130 °C by possessing both high dielectric permittivity around 5300 and low dielectric permittivity change of only ±5.9%.

$$\frac{\Delta\varepsilon_r}{\varepsilon_r(25\ ^\circ C)}=\frac{\varepsilon_r(T)-\varepsilon_r(25\ ^\circ C)}{\varepsilon_r(25\ ^\circ C)}\times 100 \tag{3}$$

Here, $\varepsilon_r(25\ ^\circ C)$ and $\varepsilon_r(T)$ represent the dielectric permittivity at 25 °C and a given temperature, respectively.

3.3. Piezoelectric and energy storage properties of 50B24h sample

A large, temperature-stable dielectric permittivity combined with low electric loss is necessary to develop high-energy-density capacitors [72]. To evaluate the energy storage performances of 50B24h ceramic, the room-temperature polarization–electric field (P–E) hysteresis loops were recorded (Fig. 3a). 50B24h ceramic shows a slim and non-saturated hysteresis loop, where the remnant polarization (P_r), the maximal polarization (P_{max}) and the coercive field (E_c) are found to be 3.08 μC/cm^2, 17.68 μC/cm^2 and 1.61 kV/cm, respectively. The slimmest hysteresis loop is characteristic of relaxor ferroelectric with fine-grained microstructure [73]. The obtained values are excellent compared to other BCZT ceramics [16,64,74,75]. Besides, the low E_c demonstrates that 50B24h ceramic is soft concerning the electric field because the free energy profile for polarization rotation is anisotropically flattened at the morphotropic phase boundary; hence the very low field is required to align the domains easily [76].

The ability of 50B24h ceramic to generate mechanical deformations from electrical power was investigated. When an electric field is imposed on the crystal, stress on its structure is induced; this property is mostly used in actuators [77]. The piezoelectric effect in 50B24h ceramic was evaluated indirectly using the strain–electric field (S–E) hysteresis loop, as presented in Fig. 3a. A symmetric butterfly-like shape is observed due to the lattice distortion and the electric field's switching and movement of domain walls [9,75,78]. Besides, a high maximum strain (S_{max}) value of 0.093% is obtained in 50B24h ceramic, which corresponds to a large-signal piezoelectric coefficient ($d^*_{33} = S_{max}/E_{max}$) of 310 pm/V, where E_{max} is the maximum electric field. At room temperature and under 25 kV/cm, Merselmiz *et al.* reported S_{max} and d^*_{33} of 0.062% and 234 pm/V, respectively, in $Ba_{0.85}Ca_{0.15}Zr_{0.1}Ti_{0.9}O_3$ [23]. Besides, at room temperature and under 30 kV/cm, Praveen *et al.* stated that BZT–52BCT ceramic exhibits d^*_{33} value of 250 pm/V [18]. Using the same conditions, Chaiyo *et al.* reported a comparable d^*_{33} value of 312 pm/V in $Ba_{0.90}Ca_{0.10}Zr_{0.15}Ti_{0.85}O_3$ ceramic [79]. Furthermore, Merselmiz *et al.* reported S_{max} and d^*_{33} of 0.055% and 218 pm/V, respectively, in $Ba_{0.80}Ca_{0.20}Zr_{0.02}Ti_{0.98}O_3$ ceramic under 25 kV/cm [9]. Accordingly, these results make 50B24h ceramic a suitable eco-friendly material for actuators applications.

The energy storage density can be easily deduced from the registered P–E hysteresis loop (Fig. 3a) by integrating the area between the polarization axis and the P–E curve [20]. As shown in Fig. 3b, the green area is equal to the recoverable energy density (W_{rec}), the red area is equivalent to the dissipated energy density (W_{loss}), and the overall area of the two parts equals the total energy density (W_{tot}). Besides, to evaluate the energy storage performances, it is required to estimate energy efficiency (η). Thus, W_{tot}, W_{rec} and η could be estimated by employing Eqs. (4)–(6), respectively [80].

Table 1
Relaxor properties of 50B24h ceramic at 1 kHz.

ε_r (at T_m)	$tan\ \delta$ (at T_m)	$C \times 10^5$ (K)	T_0 (°C)	T_m (°C)	T_{dev} (°C)	ΔT_m (°C)	γ
5300	0.03	3.39	65.3	92.6	160.6	68.0	2.13

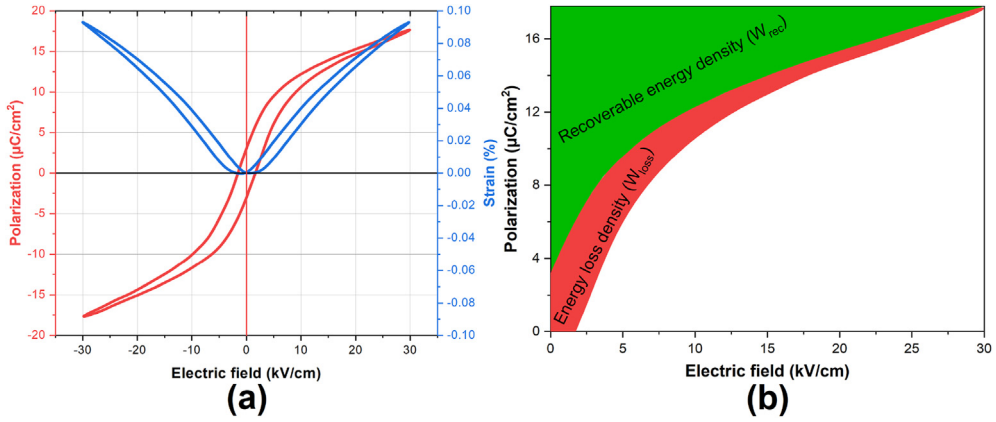

Fig. 3. Piezoelectric and energy storage properties of 50B24h ceramic. (a) Bipolar *P*–*E* and *S*–*E* hysteresis loops and (b) a schematic representation of the relevant energy storage parameters determined via *P*–*E* hysteresis loop.

Table 2
Comparison of the room-temperature energy storage properties of 50B24h ceramic with other BCZT ceramics reported in the literature.

Ceramic	Synthesis conditions			W_{tot} (mJ/cm^3)	W_{rec} (mJ/cm^3)	η (%)	E (kV/cm)	Ref.
	Method	Calcination	Sintering					
50B24h	Hydrothermal	No	1250 °C/10 h	171.6	135.6	78.9	30	This work
50B24h	Hydrothermal	No	1250 °C/10 h	344.5	262.0	76.0	60	This work
$Ba_{0.85}Ca_{0.15}Zr_{0.10}Ti_{0.90}O_3$	Hydrothermal	No	1280 °C/18 h	60.7	45.6	75.1	20	[96]
$Ba_{0.85}Ca_{0.15}Zr_{0.10}Ti_{0.90}O_3$	Solid-state	1250 °C/4 h	1350–1500 °C/10 h	113.8	38.6	33.9	20	[75]
$Ba_{0.98}Ca_{0.02}Zr_{0.02}Ti_{0.98}O_3$	Solid-state	1200 °C/3 h	1380 °C/3 h	159.0	82.0	51.5	20	[90]
$Ba_{0.85}Ca_{0.15}Zr_{0.10}Ti_{0.90}O_3$	Solid-state	1300 °C/12 h	1350 °C/7 h	202.0	75.0	37.0	25	[23]
$Ba_{0.85}Ca_{0.15}Zr_{0.10}Ti_{0.90}O_3$	Hydrothermal	No	1250 °C/10 h	227.5	161.4	70.9	30	[20]
$Ba_{0.85}Ca_{0.15}Zr_{0.10}Ti_{0.90}O_3$	Solid-state	1250 °C/10 h	1500 °C/4 h	166.0	133.0	79.8	30	[81]
$Ba_{0.85}Ca_{0.15}Zr_{0.10}Ti_{0.90}O_3$	Solid-state	1250 °C/2 h	1400 °C/2 h	130.7	67.2	51.4	30	[71]
$Ba_{0.88}Ca_{0.12}Zr_{0.12}Ti_{0.88}O_3$	Solid-state	1000 °C/2 h	1250 °C/3 h	132.0	93.7	71.0	30	[89]
$Ba_{0.95}Ca_{0.05}Zr_{0.20}Ti_{0.80}O_3$	Solid-state	1200 °C/4 h	1350 °C/2 h	100.8	78.3	77.7	30	[82]
$Ba_{0.95}Ca_{0.05}Zr_{0.20}Ti_{0.80}O_3$	Citrate precursor	650 °C/2 h	1250 °C/2 h	97.1	78.3	80.6	30	[82]
$Ba_{0.85}Ca_{0.15}Zr_{0.10}Ti_{0.90}O_3$	Sol-gel	1000 °C/4 h	1300 °C	232.5	128.8	55.4	40	[83]
$Ba_{0.90}Ca_{0.10}Zr_{0.10}Ti_{0.90}O_3$	Solid-state	1200 °C/2 h	1150 °C/2 h	1086.7	106.5	9.8	45	[88]
$Ba_{0.85}Ca_{0.15}Zr_{0.10}Ti_{0.90}O_3$	Solid-state	1200 °C/3 h	1400 °C/3 h	281.9	210.0	74.5	50	[87]
$Ba_{0.85}Ca_{0.15}Zr_{0.10}Ti_{0.90}O_3$	Sol-gel	1000 °C	1100–1300 °C/2 h	240.3	130.0	54.1	55	[86]
$Ba_{0.85}Ca_{0.15}Zr_{0.10}Ti_{0.90}O_3$	Hydrothermal	No	1250 °C/10 h	546.1	367.2	67.2	60	[20]
$Ba_{0.85}Ca_{0.15}Zr_{0.10}Ti_{0.90}O_3$	Solid-state	1200 °C	1350 °C	235.2	121.6	51.7	60	[84]
$Ba_{0.85}Ca_{0.15}Zr_{0.10}Ti_{0.90}O_3$	Solid-state	1100–1150 °C/2 h	1300–1380 °C/5 h	345.3	126.4	36.6	70	[85]

$$W_{\text{tot}} = \int_0^{P_{max}} E dP, \tag{4}$$

$$W_{\text{rec}} = \int_{P_r}^{P_{\max}} E dP, \tag{5}$$

$$\eta\ (\%) = \frac{W_{\text{rec}}}{W_{\text{tot}}} \times 100 = \frac{W_{\text{rec}}}{W_{\text{rec}} + W_{\text{loss}}} \times 100 \tag{6}$$

Table 2 compares the room-temperature energy storage properties of 50B24h ceramic with other BCZT ceramics, elaborated by different conditions of synthesis and methods, reported in the literature. In 50B24h ceramic, W_{tot} and W_{rec} are 188.2 and 140.3 mJ/cm^3, which corresponds to η of 74.5%. These values are comparable to those obtained in $Ba_{0.85}Ca_{0.15}Zr_{0.10}Ti_{0.90}O_3$ (BCZT) ceramics elaborated by hydrothermal processing, where W_{rec} and η reached 161.4 mJ/cm^3 and 70.9%, respectively, under 30 kV/cm [20]. Puli *et al.* observed an enhanced W_{rec} of 133 mJ/cm^3 with η of 79.8% at room temperature and under 30 kV/cm in BCZT ceramics elaborated by conventional solid-state reaction method [81]. Furthermore, under 25 kV/cm, Merselmiz *et al.* reported W_{rec} and η of 75 mJ/cm^3 and 37%, respectively, in BCZT [23]. Besides, under 30 kV/cm, Zhan *et al.* compared the energy storage performances of $Ba_{0.95}Ca_{0.05}Zr_{0.20}Ti_{0.80}O_3$ prepared by solid-state reaction and citrate method and stated higher η of 77.7 and 80.6%, respectively. However, two-times lower W_{rec} values were reported compared to our sample [82]. Moreover, Chen *et al.* reported enhanced energy storage parameters (W_{rec} = 128.8 mJ/cm^3 and η = 55.4% under 40 kV/cm) in BCZT ceramic elaborated using the sol-gel method [83]. More interestingly, from energy consumption view, 50B24h ceramic was elaborated at very low temperature of 180 °C, which is about 1000–1200 °C lower when compared to solid-state reaction and 500–850 °C lower when compared to sol-gel methods, respectively. Among the big advantage of the "calcination-free" in the hydrothermal processing, 50B24h exhibits enhanced energy storage properties compared to other BCZT ceramics [71,82–90].

For enhanced energy storage performances, the unipolar *P*–*E* loops of the 50B24h sample were recorded at higher electric fields (Fig. 4a). The maximal polarization and remnant polarization increase with the increasing electric field. At 60 kV/cm, P_{max} and P_r are 23.6 and 6.3 μC/cm^2, respectively. From equation (4), increasing the applied electric field boosts the energy storage density. The electric

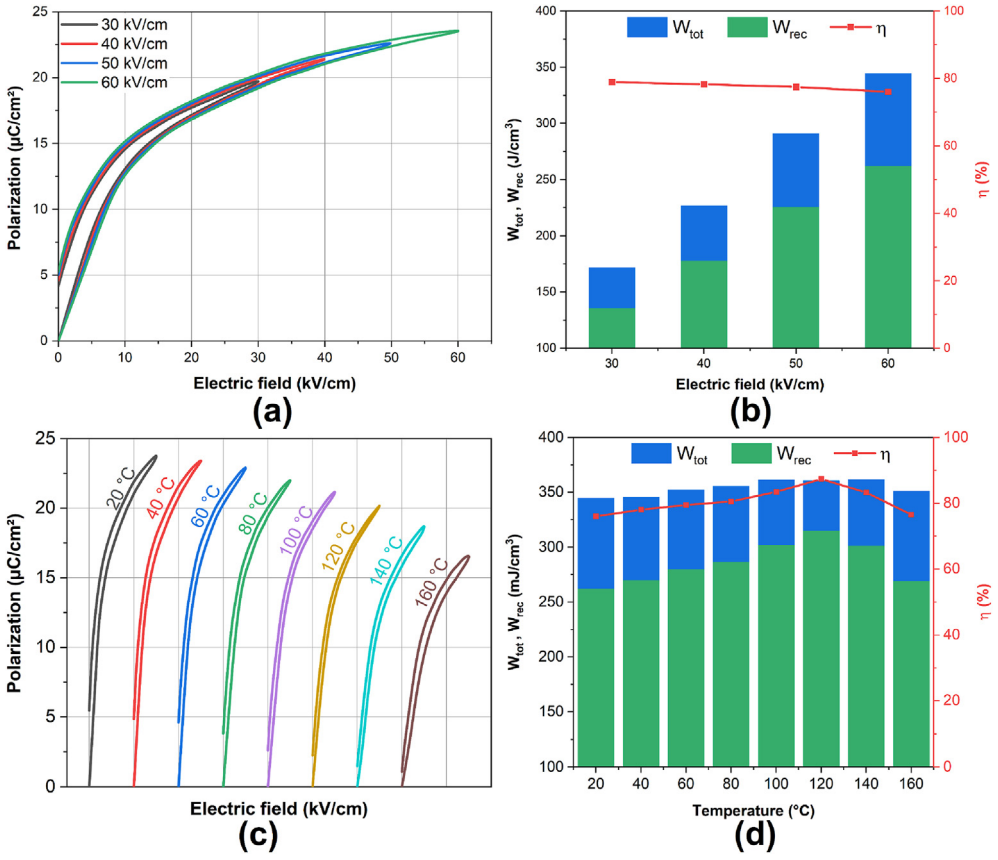

Fig. 4. Energy storage performances of 50B24h ceramic. Room-temperature (a) unipolar *P*–*E* loops at different electric fields and (b) the electric field dependence of the energy storage parameters. (c) Unipolar *P*–*E* loops at different temperatures (each *P*–*E* curve was translated by 40 kV/cm for clear visibility) and (d) the temperature dependence of the energy storage parameters at 60 kV/cm.

field dependence of the energy storage properties of 50B24h ceramic is illustrated in Fig. 4b. From 30 to 60 kV/cm, a linear behavior of the W_{tot} and W_{rec} is observed, where W_{tot} and W_{rec} increased from 171.8 and 135.6 mJ/cm^3 to 344.5 and 262.0 mJ/cm^3, respectively, with a slight decline of η (from 78.9% to 76.0%). The resulting energy storage properties are enhanced compared to those reported in [84,85]. It was stated before that the non-saturated *P*–*E* loops in BCZT ceramic allow to further increase the applied electric field, hence, enhancing the energy density. However, due to the observed porosity (Fig. 1d) and the small relative density (90%), and in order to avoid the electric breakdown at high temperatures, the electric field was kept at 60 kV/cm.

The excellent temperature stability over wide operating temperature is a vital factor for the practical application of energy storage capacitors [84,91]. For this purpose, *P*–*E* hysteresis loops of 50B24h ceramic were registered from 20 to 160 °C at 60 kV/cm and plotted in Fig. 4c. 50B24h sample always exhibits slim *P*–*E* loops in the temperature range of measurement. As the temperature increases, the *P*–*E* loops become slimmer, accompanied by the continuous decrease of P_r and P_{max}, due to the shift of the ferroelectric domain direction. Above T_C, the *P*–*E* loops do not show strictly linear behavior, characteristic of the pure paraelectric phase.

In contrast, very slim loops appeared corresponding to the existence of ferroelectric clusters or residual polar nanoregions (PNR) [92–94] due to the relaxor behavior of the 50B24h sample [51]. Accordingly, the temperature dependence of the energy storage performances of BCZT ceramic under 60 kV/cm was calculated and presented in Fig. 4d. It is observed that W_{tot}, W_{rec} and η increase gradually with temperature to reach a maximum around 120 °C then decrease. The energy parameters at 120 °C W_{tot}, W_{rec} and η are 360.6, 315.0 and 87.4%, respectively. Although the energy parameters variate with temperature, a slight energy storage variation of W_{rec} (ESV) in the temperature range of 20–160 °C of 14.9% is observed. The above results indicate the excellent thermal stability of 50B24h ceramic over a wide temperature range due to the strengthened diffuse phase transition behavior [20]. These outcomes are very promising compared to other ferroelectric materials, where a high ESV at the ferroelectric-paraelectric phase transition is usually observed [23,75,89,95].

Generally, the enhancement in energy storage density can be ascribed to the reduction in dielectric loss, an increase in dielectric constant, and improvement of electric breakdown strength. Furthermore, interfacial polarization is considered a universal phenomenon in all heterogeneous dielectric materials [55]. In our case, the differential polarization generated from the difference between BCZT and CZTO-based phases contributes to the energy storage density enhancement. Compared to the BCZT ceramics reported in the literature, which rely on high-temperature processing, 50B24h ceramic exhibits enhanced energy storage parameters at a much lower temperature. These features may offer a new strategy to tailor lead-free relaxor ferroelectrics toward superior energy storage performance for ceramic capacitor applications.

4. Conclusions

A mixed powder of nanowires, cubes and multipods was prepared using the sol-gel method followed by two-steps

hydrothermal processing. The phase transitions in 50B24h ceramic were investigated using the dielectric and Raman measurements. We demonstrated that the 50B24h ceramic shows enhanced dielectric properties with $\varepsilon_r = 5300$ and $tan\ \delta = 0.03$, low dielectric permittivity variation with $\Delta\varepsilon_r/\varepsilon_r$ of ±5.9% at 25 °C, and boosted energy storage performances with $W_{rec} = 315.0$ mJ/cm^3 mJ/cm^3 and $\eta = 87.4\%$, and the improved piezoelectric properties with $S_{max} = 0.093\%$ and $d^*_{33} = 310$ pm/V. Besides, 50B24h demonstrated excellent thermal stability with a slight variation of W_{rec} of 14.9% in the temperature range of 20–160 °C. These results are transferable to the synthesis of other complex perovskite oxides with different nanostructured morphologies and present an innovative strategy for exploring other nanostructured lead-free ceramics for energy storage and energy harvesting applications.

Declaration of competing interest

The authors declare that they have no known competing financial interests or personal relationships that could have appeared to influence the work reported in this paper.

Acknowledgements

The authors gratefully acknowledge the generous financial support of the European Union Horizon 2020 Research and Innovation actions MSCA-RISE-ENGIMA (No. 778072) and MSCA-RISE-MELON (No. 872631). Z. K., B. R., D. V., and M. S. acknowledge the Slovenian Research Agency program P1-0125 and P2-0091.

References

[1] Hong CH, Kim HP, Choi BY, Han HS, Son JS, Ahn CW, et al. J Mater 2016;2:1–24. https://doi.org/10.1016/j.jmat.2015.12.002.
[2] Panda PK, Sahoo B. Ferroelectrics 2015;474:128–43. https://doi.org/10.1080/00150193.2015.997146.
[3] Shrout TR, Zhang SJ. J Electroceram 2007;19:111–24. https://doi.org/10.1007/s10832-007-9047-0.
[4] Rödel J, Jo W, Seifert KTP, Anton EM, Granzow T, Damjanovic D. J Am Ceram Soc 2009;92:1153–77. https://doi.org/10.1111/j.1551-2916.2009.03061.x.
[5] Jin CC, Liu XC, Liu CH, Wang Y, Hwang HL, Wang Q. Mater Des 2018;144:55–63. https://doi.org/10.1016/j.matdes.2018.02.008.
[6] Bera Binoy. Imp J Interdiscip Res 2016;2:1274–91.
[7] Si SK, Karan SK, Paria S, Maitra A, Das AK, Bera R, et al. Mater Chem Phys 2018;213:525–37. https://doi.org/10.1016/j.matchemphys.2018.04.013.
[8] Priya S, Nahm S. New York, NY: springer New York. https://doi.org/10.1007/978-1-4419-9598-8; 2013. 9781441995.
[9] Merselmiz S, Hanani Z, Ben Moumen S, Matavž A, Mezzane D, Novak N, et al. J Mater Sci Mater Electron 2020;31:17018–28. https://doi.org/10.1007/s10854-020-04259-w.
[10] Dong X, Li X, Chen X, Chen H, Sun C, Shi J, et al. J Mater 2021;7:629–39. https://doi.org/10.1016/j.jmat.2020.11.016.
[11] Koruza J, Bell AJ, Frömling T, Webber KG, Wang K, Rödel J. J Mater 2018;4:13–26. https://doi.org/10.1016/j.jmat.2018.02.001.
[12] Zhao C, Huang Y, Wu J. InfoMat 2020;2:1163–90. https://doi.org/10.1002/inf2.12147.
[13] Lv X, Zhu J, Xiao D, Zhang XX, Wu J. Chem Soc Rev 2020;49:671–707. https://doi.org/10.1039/c9cs00432g.
[14] Liu W, Ren X. Phys Rev Lett 2009;103:257602. https://doi.org/10.1103/PhysRevLett.103.257602.
[15] Hanani Z, Mezzane D, Amjoud M, Razumnaya AG, Fourcade S, Gagou Y, et al. J Mater Sci Mater Electron 2019;30:6430–8. https://doi.org/10.1007/s10854-019-00946-5.
[16] Hanani Z, Mezzane D, Amjoud M, Gagou Y, Hoummada K, Perrin C, et al. J Mater Sci Mater Electron 2020;31:10096–104. https://doi.org/10.1007/s10854-020-03555-9.
[17] Maraj M, Wei W, Peng B, Sun W. Materials (Basel) 2019;12:3641. https://doi.org/10.3390/ma12213641.
[18] Praveen JP, Karthik T, James AR, Chandrakala E, Asthana S, Das D. J Eur Ceram Soc 2015;35:1785–98. https://doi.org/10.1016/j.jeurceramsoc.2014.12.010.
[19] Wu J, Xiao D, Wu W, Chen Q, Zhu J, Yang Z, et al. J Eur Ceram Soc 2012;32:891–8. https://doi.org/10.1016/j.jeurceramsoc.2011.11.003.
[20] Hanani Z, Merselmiz S, Mezzane D, Amjoud M, Bradeško A, Rožič B, et al. RSC Adv 2020;10:30746–55. https://doi.org/10.1039/d0ra06116f.
[21] Hanani Z, Izanzar I, Amjoud M, Mezzane D, Lahcini M, Uršič H, et al. Nano Energy 2021;81:105661. https://doi.org/10.1016/j.nanoen.2020.105661.
[22] Hanani Z, Ablouh EH, Amjoud M 'barek, Mezzane D, Fourcade S, Gouné M. Ceram Int 2018;44:10997–1000. https://doi.org/10.1016/j.ceramint.2018.03.022.
[23] Merselmiz S, Hanani Z, Mezzane D, Razumnaya AG, Amjoud M, Hajji L, et al. RSC Adv 2021;11:9459–68. https://doi.org/10.1039/D0RA09707A.
[24] Bai Y, Matousek A, Tofel P, Bijalwan V, Nan B, Hughes H, et al. J Eur Ceram Soc 2015;35:3445–56. https://doi.org/10.1016/j.jeurceramsoc.2015.05.010.
[25] Hanani Z, Merselmiz S, Danine A, Stein N, Mezzane D, Amjoud M, et al. J Adv Ceram 2020;9:210–9. https://doi.org/10.1007/s40145-020-0361-1.
[26] Koka A, Zhou Z, Sodano HA. Energy Environ Sci 2014;7:288–96. https://doi.org/10.1039/c3ee42540a.
[27] Wu W, Cheng L, Bai S, Dou W, Xu Q, Wei Z, et al. J Mater Chem A 2013;1:7332–8. https://doi.org/10.1039/c3ta10792b.
[28] Alexe M, Hesse D. Ferroelectrics 2012;433:53–64. https://doi.org/10.1080/07399332.2012.678120.
[29] Bao N, Shen L, Srinivasan G, Yanagisawa K, Gupta A. J Phys Chem C 2008;112:8634–42. https://doi.org/10.1021/jp802055a.
[30] Hu D, Yao M, Fan Y, Ma C, Fan M, Liu M. Nano Energy 2019;55:288–304. https://doi.org/10.1016/j.nanoen.2018.10.053.
[31] Zhou Z, Bowland CC, Malakooti MH, Tang H, Sodano HA. Nanoscale 2016;8:5098–105. https://doi.org/10.1039/c5nr09029f.
[32] Chary KS, Panda HS, Prasad CD. Ind Eng Chem Res 2017;56:10335–42. https://doi.org/10.1021/acs.iecr.7b02182.
[33] Datta A, Sanchez-Jimenez PE, Al Orabi RAR, Calahorra Y, Ou C, Sahonta SL, et al. Adv Funct Mater 2017;27:1701169. https://doi.org/10.1002/adfm.201701169.
[34] Chen J, Chen X, He F, Wang Y, Zhou H, Fang L. J Electron Mater 2014;43:1112–8. https://doi.org/10.1007/s11664-014-3030-8.
[35] Ren P, Wang J, He J, Wang Y, Yuan H, Hao Y, et al. Adv Electron Mater 2020;6:1901429. https://doi.org/10.1002/aelm.201901429.
[36] Jia W, Hou Y, Zheng M, Xu Y, Yu X, Zhu M, et al. J Am Ceram Soc 2018;101:3468–79. https://doi.org/10.1111/jace.15519.
[37] Li WB, Zhou D, Liu WF, Su JZ, Hussain F, Wang DW, et al. Chem Eng J 2021;414:128760. https://doi.org/10.1016/j.cej.2021.128760.
[38] Liu G, Li Y, Shi M, Yu L, Chen P, Yu K, et al. Ceram Int 2019;45:19189–96. https://doi.org/10.1016/j.ceramint.2019.06.166.
[39] Yang H, Lu Z, Li L, Bao W, Ji H, Li J, et al. ACS Appl Mater Interfaces 2020;12:43942–9. https://doi.org/10.1021/acsami.0c13057.
[40] Zhou S, Pu Y, Zhang X, Shi Y, Gao Z, Feng Y, et al. Chem Eng J 2022;427:131684. https://doi.org/10.1016/j.cej.2021.131684.
[41] Yang H, Bao W, Lu Z, Li L, Ji H, Huang Y, et al. J Mater Res 2021;36:1285–94. https://doi.org/10.1557/s43578-020-00093-2.
[42] Li WB, Zhou D, Xu R, Wang DW, Su JZ, Pang LX, et al. ACS Appl Energy Mater 2019;2:5499–506. https://doi.org/10.1021/acsaem.9b00664.
[43] Hanani Z, Ablouh EH, Merselmiz S, Ghanbaja J, Amjoud M, Mezzane D, et al. CrystEngComm 2021;23:5249–56. https://doi.org/10.1039/d1ce00591j.
[44] Zhang J, Wang J, Gao D, Liu H, Xie J, Hu W. J Eur Ceram Soc 2021;41:352–9. https://doi.org/10.1016/j.jeurceramsoc.2020.09.017.
[45] Zhou HY, Liu XQ, Zhu XL, Chen XM. J Am Ceram Soc 2018;101:1999–2008. https://doi.org/10.1111/jace.15371.
[46] Zhou HY, Zhu XN, Ren GR, Chen XM. J Alloys Compd 2016;688:687–91. https://doi.org/10.1016/j.jallcom.2016.07.078.
[47] Lee H, Kim JR, Lanagan MJ, Trolier-Mckinstry S, Randall CA. J Am Ceram Soc 2013;96:1209–13. https://doi.org/10.1111/jace.12184.
[48] Shay DP, Randall CA. SAE Tech Pap 2012;10. https://doi.org/10.4271/2012-01-2208. 2012-01–2208.
[49] Tenne DA, Xi XX, Li YL, Chen LQ, Soukiassian A, Zhu MH, et al. Phys Rev B Condens Matter 2004;69:174101. https://doi.org/10.1103/PhysRevB.69.174101.
[50] Coondoo I, Panwar N, Krylova S, Krylov A, Alikin D, Jakka SK, et al. Ceram Int 2021;47:2828–38. https://doi.org/10.1016/j.ceramint.2020.09.137.
[51] Shi J, Zhu R, Liu X, Fang B, Yuan N, Ding J, et al. Materials (Basel) 2017;10:1093. https://doi.org/10.3390/ma10091093.
[52] Zeng WY, Anderson A. J Raman Spectrosc 2001;32:69–71. https://doi.org/10.1002/1097-4555(200101)32:1<69::AID-JRS673>3.0.CO;2-3.
[53] Wang Z, Wang J, Chao X, Wei L, Yang B, Wang D, et al. J Mater Sci Mater Electron 2016;27:5047–58. https://doi.org/10.1007/s10854-016-4392-x.
[54] Hanani Z, Mezzane D, Amjoud M, Fourcade S, Razumnaya AG, Luk'yanchuk IA, et al. Superlattice Microst 2019;127:109–17. https://doi.org/10.1016/j.spmi.2018.03.004.
[55] Ma W, Zhu Y, Marwat MA, Fan P, Xie B, Salamon D, et al. J Mater Chem C 2019;7:281–8. https://doi.org/10.1039/c8tc04447c.
[56] Zhao C, Wu H, Li F, Cai Y, Zhang Y, Song D, et al. J Am Chem Soc 2018;140:15252–60. https://doi.org/10.1021/jacs.8b07844.
[57] Zhang MH, Wang K, Zhou JS, Zhou JJ, Chu X, Lv X, et al. Acta Mater 2017;122:344–51. https://doi.org/10.1016/j.actamat.2016.10.011.
[58] Bokov AA, Ye ZG. Front. Ferroelectr. A Spec. Issue J. Mater. Sci. Boston, MA: Springer US; 2007. p. 31–52. https://doi.org/10.1007/978-0-387-38039-1_4.
[59] Liu Y, Pu Y, Sun Z. Mater Lett 2014;137:128–31. https://doi.org/10.1016/j.matlet.2014.08.138.
[60] Merselmiz S, Hanani Z, Mezzane D, Spreitzer M, Bradeško A, Fabijan D, et al. Ceram Int 2020;46:23867–76. https://doi.org/10.1016/j.ceramint.2020.06.163.
[61] Uchino K, Nomura S. Ferroelectrics Lett 1982;44:55–61. https://doi.org/10.1080/07315178208201875.

[62] Jan SQ, Usman M, Naveed-Ul-Haq M, Mumtaz A. J Alloys Compd 2018;735:1893–900. https://doi.org/10.1016/j.jallcom.2017.11.275.
[63] Xi K, Li Y, Zheng Z, Zhang L, Liu Y, Mi Y. J Mater Sci Mater Electron 2020;31:23044–51. https://doi.org/10.1007/s10854-020-04832-3.
[64] Ji X, Wang C, Harumoto T, Zhang S, Tu R, Shen Q, et al. Sci Rep 2020;10:20352. https://doi.org/10.1038/s41598-020-73784-9.
[65] Schmidt VH, Archer N, Tu CS. J Am Ceram Soc 2018;101:713–22. https://doi.org/10.1111/jace.15236.
[66] Cui L, Hou YD, Wang S, Wang C, Zhu MK. J Appl Phys 2010;107:054105. https://doi.org/10.1063/1.3327244.
[67] Jiang X, Hao H, Yang Y, Zhou E, Zhang S, Wei P, et al. J Mater 2021;7:295–301. https://doi.org/10.1016/j.jmat.2020.09.001.
[68] Ma D, Chen X, Huang G, Chen J, Zhou H, Fang L. Ceram Int 2015;41:7157–61. https://doi.org/10.1016/j.ceramint.2015.02.036.
[69] Dong X, Chen X, Chen H, Sun C, Shi J, Pang F, et al. J Mater Sci Mater Electron 2020;31:22780–8. https://doi.org/10.1007/s10854-020-04802-9.
[70] Jeon SC, Yoon BK, Kim KH, Kang SJL. J Adv Ceram 2014;3:76–82. https://doi.org/10.1007/s40145-014-0096-y.
[71] Zhou M, Liang R, Zhou Z, Xu C, Nie X, Chen X, et al. Mater Res Bull 2018;98:166–72. https://doi.org/10.1016/j.materresbull.2017.10.005.
[72] Hao X. J Adv Dielectr 2013;3:1330001. https://doi.org/10.1142/s2010135x13300016.
[73] Lu B, Li P, Tang Z, Yao Y, Gao X, Kleemann W, et al. Sci Rep 2017;7:45335. https://doi.org/10.1038/srep45335.
[74] Hunpratub S, Maensiri S, Chindaprasirt P. Ceram Int 2014;40:13025–31. https://doi.org/10.1016/j.ceramint.2014.04.166.
[75] Cai W, Zhang Q, Zhou C, Gao R, Zhang S, Li Z, et al. J Mater Sci Mater Electron 2020;31:9167–75. https://doi.org/10.1007/s10854-020-03446-z.
[76] Praveen JP, Kumar K, James AR, Karthik T, Asthana S, Das D. Curr Appl Phys 2014;14:396–402. https://doi.org/10.1016/j.cap.2013.12.026.
[77] Rödel J, Webber KG, Dittmer R, Jo W, Kimura M, Damjanovic D. J Eur Ceram Soc 2015;35:1659–81. https://doi.org/10.1016/j.jeurceramsoc.2014.12.013.
[78] Obilor U, Pascual-Gonzalez C, Murakami S, Reaney IM, Feteira A. Mater Res Bull 2018;97:385–92. https://doi.org/10.1016/j.materresbull.2017.09.032.
[79] Chaiyo N, Cann DP, Vittayakorn N. J Mater Sci 2015;50:6171–9. https://doi.org/10.1007/s10853-015-9174-y.
[80] Li D, Lin Y, Yuan Q, Zhang M, Ma L, Yang H. J Mater 2020;6:743–50. https://doi.org/10.1016/j.jmat.2020.06.005.
[81] Puli VS, Pradhan DK, Coondoo I, Panwar N, Adireddy S, Luo S, et al. J Phys D Appl Phys 2019;52:255304. https://doi.org/10.1088/1361-6463/ab161a.
[82] Zhan D, Xu Q, Huang DP, Liu HX, Chen W, Zhang F. J Phys Chem Solid 2018;114:220–7. https://doi.org/10.1016/j.jpcs.2017.10.038.
[83] Chen Y, Chen D, Meng L, Wan L, Yao H, Zhai J, et al. R Soc Open Sci 2020;7:191822. https://doi.org/10.1098/rsos.191822.
[84] Xu K, Yang P, Peng W, Li L. J Alloys Compd 2020;829:154516. https://doi.org/10.1016/j.jallcom.2020.154516.
[85] Dai Z, Xie J, Chen Z, Zhou S, Liu J, Liu W, et al. Chem Eng J 2021;410:128341. https://doi.org/10.1016/j.cej.2020.128341.
[86] Wang XW, Zhang BH, Shi YC, Li YY, Manikandan M, Shang SY, et al. J Appl Phys 2020;127:074103. https://doi.org/10.1063/1.5138948.
[87] Gao M, Ge W, Li X, Yuan H, Liu C, Zhao H, et al. Phys Status Solidi Appl Mater Sci 2020;217:2000253. https://doi.org/10.1002/pssa.202000253.
[88] Kushvaha DK, Rout SK, Tiwari B. J Alloys Compd 2019;782:270–6. https://doi.org/10.1016/j.jallcom.2018.12.196.
[89] Jayakrishnan AR, Alex KV, Thomas A, Silva JPB, Kamakshi K, Dabra N, et al. Ceram Int 2019;45:5808–18. https://doi.org/10.1016/j.ceramint.2018.11.250.
[90] Kumari S, Kumar A, Kumar V, Dubey SK, Goyal PK, Kumar S, et al. Res Sq 2021. https://doi.org/10.1007/s10854-021-06252-3.
[91] Di H, Zhongbin P, Lukang W, Fan Y, Luomeng T, Jinghao Z, et al. J Mater 2021;7:869–78. https://doi.org/10.1016/j.jmat.2020.12.006.
[92] Ramesh G, Ramachandra Rao MS, Sivasubramanian V, Subramanian V. J Alloys Compd 2016;663:444–8. https://doi.org/10.1016/j.jallcom.2015.11.028.
[93] Eric Cross L. Ferroelectrics 1987;76:241–67. https://doi.org/10.1080/00150198708016945.
[94] Tsukada S, Akishige Y, Kim TH, Kojima S. IOP Conf Ser Mater Sci Eng 2014;54:12005. https://doi.org/10.1088/1757-899X/54/1/012005.
[95] Liu Z, Chen X, Peng W, Xu C, Dong X, Cao F, et al. Appl Phys Lett 2015;106:262901. https://doi.org/10.1063/1.4923373.
[96] Ji W, Fang B, Lu X, Zhang S, Yuan N, Ding J. Phys B Condens Matter 2019;567:65–78. https://doi.org/10.1016/j.physb.2019.02.058.

Zouhair Hanani (AMRSC) obtained his Ph.D. in Physical Chemistry of Materials and Energy in 2020 at University of Bordeaux (France) and Cadi Ayyad University (Morocco). Currently, he is a Postdoctoral researcher at Advanced Materials Department, Jožef Stefan Institute (Slovenia). His main research interests are focused on the design of architectured ferroelectric ceramics with different morphologies and compositions for energy storage, solid-state electrocaloric cooling, ceramic/polymer nanocomposites for energy storage applications, and flexible piezoelectric nanogenerators for mechanical energy harvesting.